Geophys. J. Int. (2004) doi: 10.1111/j.1365-246X.2004.02371.x

A surface wave analysis of seismic anisotropy beneath eastern North America

James B. Gaherty

Lamont–Doherty Earth Observatory of Columbia University, PO Box 1000, 61 *Route* 9W, *Palisades, NY* 10964-1000*, USA.*
E-mail: gaherty@ldeo.columbia.edu

Accepted 2004 May 17. Received 2004 May 17; in original form 2003 July 12

SUMMARY

The nature of upper-mantle seismic anisotropy beneath central and eastern North America has been evaluated using the phase velocities of surface waves traversing the length of the Missouri-to-Massachusetts (MOMA) broad-band array. Frequency-dependent phase delays of fundamental-mode Love and Rayleigh waves, measured across the array using a cross-correlation procedure, require the presence of anisotropy in the upper mantle. 2-D radially anisotropic structures obtained via linearized inversion of these data contain shear anisotropy with a magnitude of ∼3 per cent between the Moho and at least 180-km depth. Models in which the mantle lithosphere is isotropic cannot satisfy the data. This anisotropy is approximately constant across the tectonic transition from the craton to the Atlantic margin. Forward models consisting of a shallow, lithospheric layer of azimuthal anisotropy derived from previous shear wave splitting observations fail to satisfy the surface wave delay times. The combined surface wave and splitting results suggest the presence of two layers of anisotropy: a lithospheric layer that produces the phase-delay differences observed in Love and Rayleigh waves but is transparent to vertically propagating shear body waves; and a deeper (presumably asthenospheric) layer that generates the shear wave splitting. One plausible model is that the lithosphere is characterized by vertically heterogeneous anisotropic fabric, which would produce minimal splitting in vertical shear waves. Such fabric has been hypothesized for regions of weak and complex splitting such as South Africa and Australia; the results here imply that it may be appropriate for North America as well.

Key words: North America, seismic anisotropy, surface waves, upper mantle.

1 INTRODUCTION

1.1 Seismic anisotropy beneath the continents

The velocities of seismic waves that sample the upper mantle of the Earth are dependent on the direction of wave polarization and/or propagation, i.e. they are anisotropic. This anisotropy is apparent in various types of seismic data (e.g. Forsyth 1975; Shearer & Orcutt 1986; Montagner & Tanimoto 1991; Yu & Park 1994; Gaherty *et al.* 1999; Schulte-Pelkum *et al.* 2001) and it is generally believed to arise from the lattice-preferred orientation (LPO) of olivine and pyroxene in mantle rocks (e.g. Nicolas & Christensen 1987). Numerical and experimental data imply that this fabric is generated during shear deformation associated with mantle flow (Ribe 1992; Zhang & Karato 1995; Bystricky *et al.* 2000; Kaminski & Ribe 2002) and the anisotropy observations thus provide unique constraints on the dynamic state and geological history of the upper mantle.

While the mechanisms underlying seismic anisotropy are accepted, its interpretation in terms of current mantle flow and/or old geological structures remains controversial, especially in stable continental regions (e.g. Vinnik *et al.* 1992, 1995; Silver 1996; Debayle & Kennett 2000a,b; Silver *et al.* 2001; Simons *et al.* 2002). Two scenarios are envisioned: (i) the anisotropic fabric is predominantly lithospheric and is associated with ancient geological processes (e.g. Gaherty & Jordan 1995; Silver 1996); and (ii) the anisotropic fabric is maintained by shear deformation in the asthenosphere as a result of mantle convection (e.g. Vinnik *et al.* 1992; Debayle & Kennett 2000a,b). The controversy arises at least in part because either process may be important in any given location (e.g. Fouch *et al.* 2000; Simons *et al.* 2002), but it is exacerbated by the limited spatial and/or depth resolution of current observations.

The most common technique for analysing upper-mantle anisotropy in continental regions is shear wave splitting (Vinnik *et al.* 1992; Silver 1996). In this analysis, near-vertical (e.g. *S, SKS*) body waves with polarization-dependent arrival times are interpreted in the context of a single, homogeneous anisotropic layer beneath the recording station (a small number of studies have extended this analysis to two or more layers, e.g. Silver & Savage 1994; Rümpker & Silver 1998; Levin *et al.* 1999, 2000). The anisotropy is characterized by two parameters. The observed splitting time represents the time lag between the fast and slow polarizations of the split shear

wave and corresponds to the magnitude of the elastic anisotropy integrated over the anisotropic layer thickness. The fast direction represents the azimuth of the fast-wave polarization and is usually interpreted as the preferred orientation of the underlying olivine fabric (e.g. Silver 1996). The precise depth of this layer beneath the station is arbitrary, although it can be estimated in cases where nearby stations show substantial variations in splitting parameters (e.g. Alsina & Snieder 1995). In general, however, interpretation of these observations relies on comparison of fast directions with plausible deformation mechanisms such as absolute plate motion (e.g. Vinnik *et al.* 1992), tectonic fabric (e.g. Silver & Chan 1991; Silver 1996; Simons & van der Hilst 2003) and/or forward models of mantle deformation (e.g. Fouch *et al.* 2000).

The other common approach for assessing upper-mantle anisotropy is to utilize surface wave velocities. Anisotropy manifests itself in surface wave velocities in two ways: the so-called Love–Rayleigh (LR) discrepancy, where Love and Rayleigh wave velocities or traveltimes are found to be mutually incompatible with a single isotropic model; and azimuthal variations of Rayleigh wave velocities. In contrast to vertical shear wave splitting, surface wave velocities have good depth resolution through the upper mantle but are hampered by poor lateral resolution. While large-scale patterns of anisotropy have been inferred on a global scale (Montagner *et al.* 2000; Montagner 2002; Gung *et al.* 2003), more detailed estimates of anisotropy and its association with continental geology have been limited to a few regions with exceptional source and/or receiver geometries (e.g. Gaherty & Jordan 1995; Debayle & Kennett 2000a,b; Freybourger *et al.* 2001; Simons *et al.* 2002; Li *et al.* 2003). Even in these studies, the lateral resolution of anisotropy is substantially worse than that obtained with shear wave splitting analyses in regions of dense station coverage.

1.2 The Missouri-to-Massachusetts transect

The Missouri-to-Massachusetts (MOMA) seismic experiment provides an excellent opportunity to improve our understanding of upper-mantle anisotropy beneath the North American continent. This 16-month experiment consisted of 18 temporary broad-band seismic instruments deployed along a profile between permanent stations CCM and HRV of the IRIS Global Seismic Network (GSN), with a nominal station spacing of 100 km (Fig. 1; Fouch *et al.* 2000). In previous analyses, seismic recordings from these stations were used to construct a detailed portrait of upper-mantle structure beneath the transect. West of the Appalachian mountains, structure is characterized by a high-velocity, thick (∼200 km) lithosphere underlain by a weak low-velocity zone (LVZ) that may terminate near 320-km depth. Crossing the Appalachians, the lithosphere thins to less than 100 km and the underlying LVZ is much more prominent (van der Lee 2002; Li *et al.* 2003), with a possible sharp base at a depth of 270–280 km (Li *et al.* 2002). For the purposes of this discussion, we refer to the thick lithosphere region west of the Appalachians as the craton and the thin-lithosphere, eastern region as the margin; the Appalachians mark the transition (Fig. 1).

The anisotropic character of the upper mantle beneath the profile has been inferred from teleseismic shear wave splitting (Fouch *et al.* 2000). The splitting observations are remarkably coherent between adjacent stations and the splitting can be summarized in three groups (Fig. 1). On the craton, splitting times are approximately

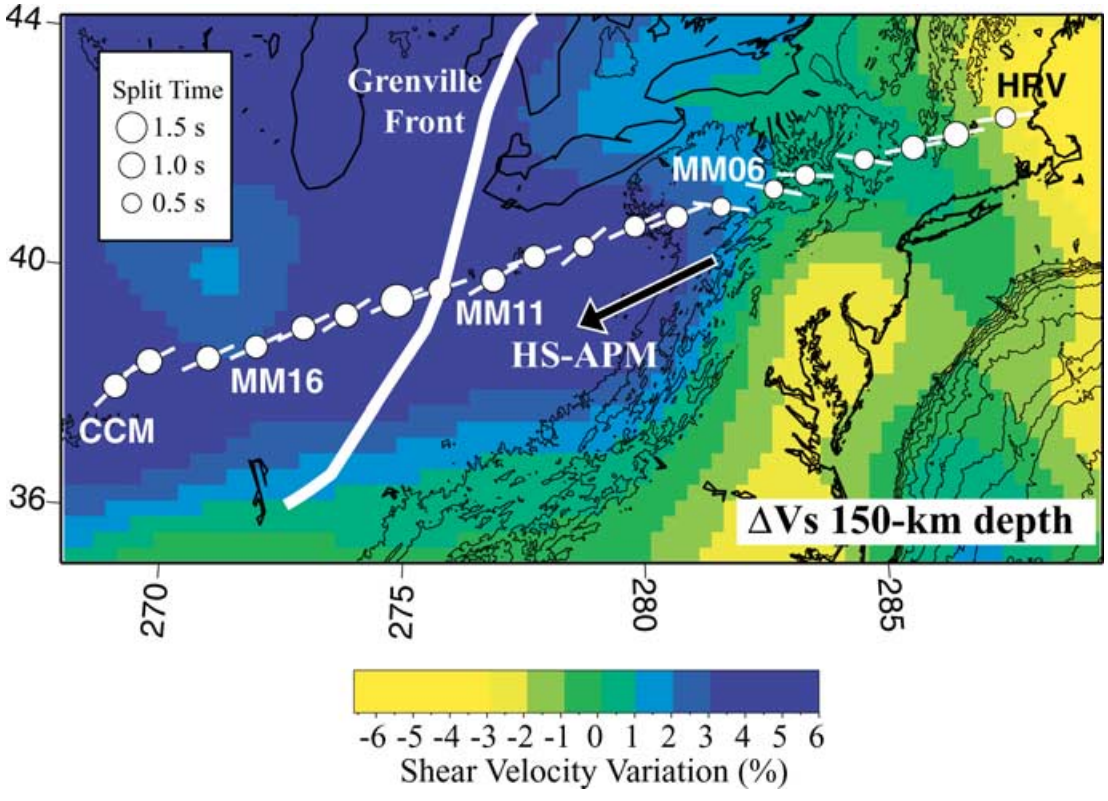

Figure 1. Shear wave splitting observations along the MOMA array (Fouch *et al.* 2000), superimposed on map of shear velocity perturbations at 150-km depth (relative to a reference velocity of 4.5 km s^{-1}) from model NA00 of van der Lee (2002). HS-APM (large arrow) gives the motion of North America with respect to a hotspot reference frame (Gripp & Gordon 1990). Fast directions (bars) in this region not only match the predictions of plate-motion-induced shear, but they are invariant across the Grenville front, a major geological boundary. Topography is contoured at 400-m intervals.

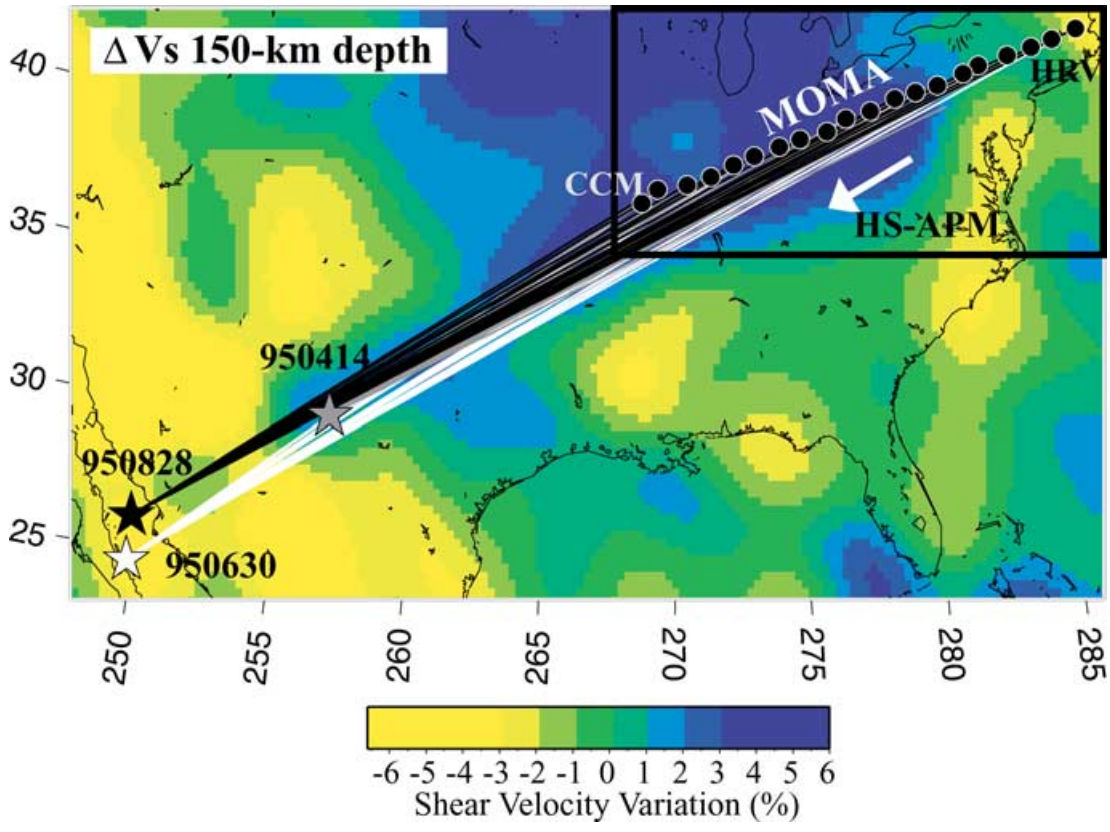

Figure 2. Surface wave ray paths used in this analysis, which propagate along the MOMA array from three earthquakes in western North America in 1995: the Mw 5.7 west Texas event of April 14 (grey star) and two events from the GoC [Mw 6.0 on June 30 (white star) and Mw 6.4 on August 21 (black star)]. Background shows shear velocity perturbations at 150-km depth relative to a reference velocity of 4.5 km s^{-1} from NA00 (van der Lee 2002). HS-APM (white arrow) represents absolute plate motion in a hotspot reference frame (Gripp & Gordon 1990). Box in upper right denotes region displayed in Fig. 1.

0.90 s and the fast polarization direction is approximately 65°, roughly parallel to absolute plate motion in a hotspot reference frame (HS-absolute plate motion (APM); Gripp & Gordon 1990). Crossing the Appalachians, the splitting times are smaller (0.45–0.65 s) and the fast direction rotates to slightly south of east. On the margin, the splitting times are larger (∼1 s) and the fast direction is dominantly E–W. By modelling these and other observations from eastern North America, Fouch *et al.* (2000) conclude that the anisotropy reflects plate-motion-induced shear in the asthenosphere beneath and around the continental tectosphere. A lithospheric component to the anisotropy cannot be ruled out, particularly beneath northeastern regions where large-scale tectonic fabric correlates with plate motion (e.g. Barruol *et al.* 1997) and where Levin *et al.* (2000) argue for two layers of anisotropy. Much of this uncertainty results from the lack of depth resolution of splitting data.

In this paper, we further characterize anisotropy beneath eastern North America by incorporating surface wave constraints. During the MOMA deployment, three earthquakes in western North America produced surface waves that traversed nearly along the axis of the array. Using phase delays of Love and Rayleigh waves measured along the array, we evaluate the depth distribution and nature of anisotropy beneath it.

2 SURFACE WAVE TRAVELTIMES

We analyse traveltimes of surface waves from three moderate-sized earthquakes: an Mw 5.7 event in west Texas (95041400) and two events from the Gulf of California (GoC; 95063011, Mw 6.0, and 95082810, Mw 6.4) (Fig. 2). For each event, we collected broadband three-component seismograms recorded at CCM, HRV and the MOMA stations. Epicentral distances range from 8–36° and source–receiver azimuths are between 45–52°. The seismograms were rotated into the receiver–source coordinate system and low-pass, zero-phase filtered with a corner at 45 mHz. All waveforms were inspected by comparing to full synthetics in two frequency windows (5–15 and 10–45 mHz) and within a given window we rejected data with signal-to-noise (S/N) ratio less than approximately two. Synthetic seismograms were calculated for a spherically symmetric Earth model using a normal-mode technique, assuming source locations and mechanisms obtained from the Harvard CMT catalogue, and were convolved with the appropriate instrument responses and filtered like the data. In general, all three events produced high S/N ratio Rayleigh waves across this frequency band. The two GoC events also produced high S/N ratio Love waves. The Texas event produced very few acceptable Love waves as a result of an unfavourable focal mechanism. Site noise (primarily at MM10–15) resulted in the elimination of some data at the lowest frequencies (5–10 mHz). The MOMA data are of excellent quality in the 15–45-mHz frequency band, often comparable to HRV and CCM (Fig. 3).

We measured frequency-dependent traveltimes of these data using a cross-correlation analysis (Gee & Jordan 1992; Gaherty *et al.* 1996). This methodology utilizes synthetic seismograms of a target wavegroup (in this case the fundamental-mode surface waves) to estimate phase delays of the observed arrival relative to the synthetic as a function of frequency. The synthetic wavegroup, called an

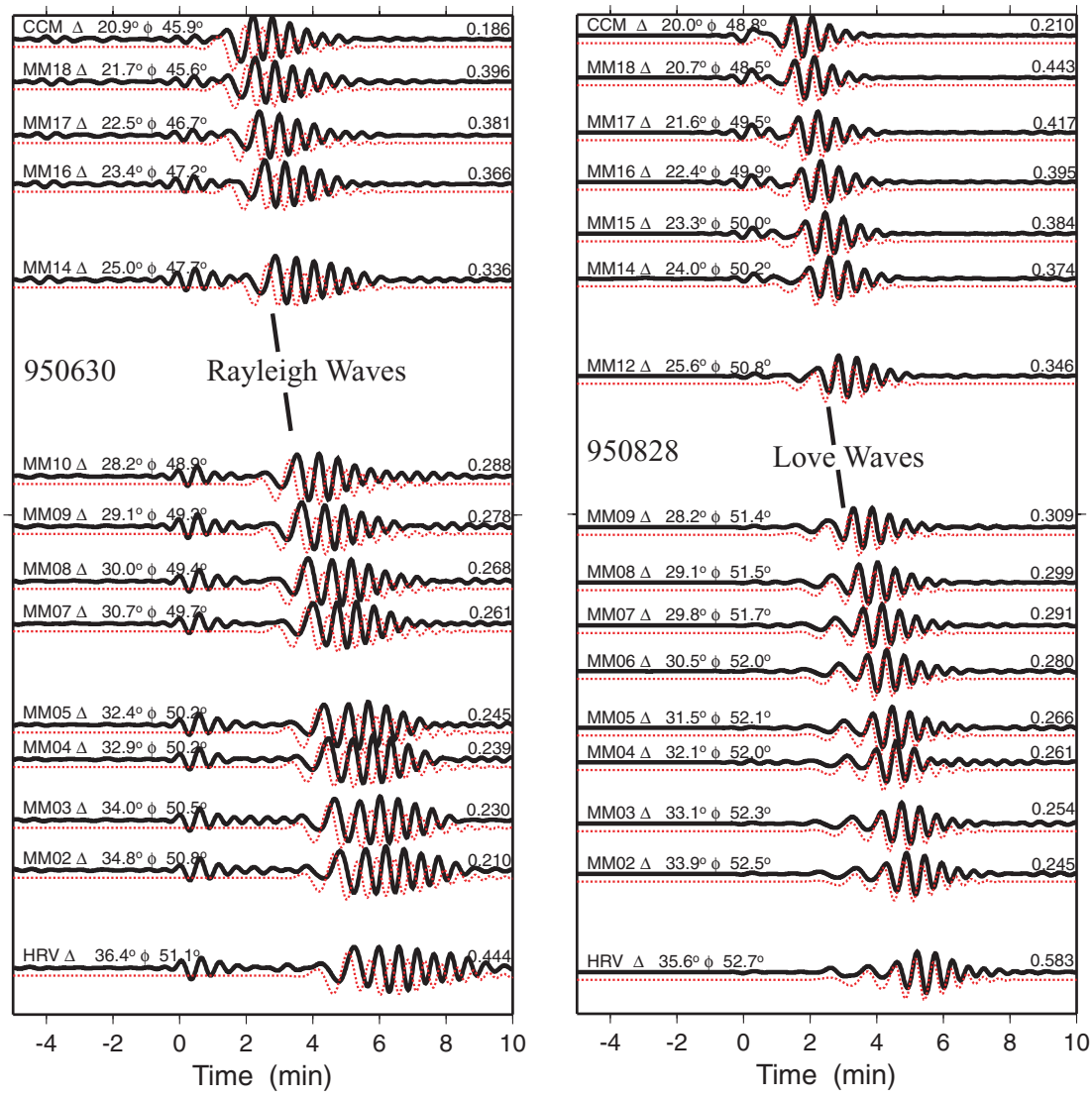

Figure 3. Example seismograms from the two GoC events. Left panel contains vertical component seismograms, while right shows tangential component. Black traces are data, while red (dotted) traces are synthetic seismograms for fundamental-mode Rayleigh and Love waves for the 1-D radially anisotropic model CUS, which is shown in Fig. 4. The seismograms were low-pass, zero-phase filtered with a corner at 45 mHz. Synthetic seismograms have been convolved with the instrument response for the appropriate station and filtered like the data. Ground motion amplitude is in digital units and each seismogram has been scaled by its maximum amplitude.

isolation filter, is cross-correlated with both the data and a complete synthetic seismogram. The resulting cross-correlagrams are windowed and narrow-band (Gaussian) filtered at discrete frequency intervals (5, 7, 10, 15, 20, 25, 30 and 40 mHz) and the phase of each correlagram is estimated at each frequency. The phase delays are calculated by subtracting each synthetic-/isolation-filter phase from the corresponding data-/isolation-filter phase (referencing the observations to a synthetic-/isolation-filter cross-correlation allows us to account for interference from unmodelled wave groups and minimizes bias associated with windowing and filtering). We also calculate the sensitivity kernel associated with each phase delay. These kernels are specific to each observation and account for interference from unmodelled phases (Gaherty *et al.* 1996). Such interference is small in the data considered here and the kernels are very similar to standard fundamental-mode surface wave kernels (e.g. Nolet *et al.* 1986). We applied this analysis to all Love and Rayleigh waves with acceptable S/N ratio. Each observation provides sensitivity to path-average crustal and mantle structure. In general, the two highest frequencies are dominated by the structure of the crust, the 15–25 mHz bands are sensitive mostly to the mantle lithosphere and the lowest three frequencies provide sensitivity in the underlying asthenosphere, down to approximately 350-km depth (Fig. 4).

Initial phase-delay measurements were made using synthetic seismograms calculated for an isotropic model, IASP91, with a modified crustal structure appropriate for these source–receiver paths (Laske *et al.* 2001; Li *et al.* 2002). The resulting delay times were quite large, with a substantial LR discrepancy (Love waves much faster than Rayleigh waves). We therefore opted to invert these data for a single, path-average reference model (dubbed chosen model name) for the subsequent analyses (Fig. 4). Improving the fit to both the Love and Rayleigh waves required the introduction of ∼3 per cent radial anisotropy similar to that contained in preliminary reference Earth model PREM (e.g. Dziewonski & Anderson 1981; Ekström & Dziewonski 1998; Gaherty *et al.* 1999), as well as a modest

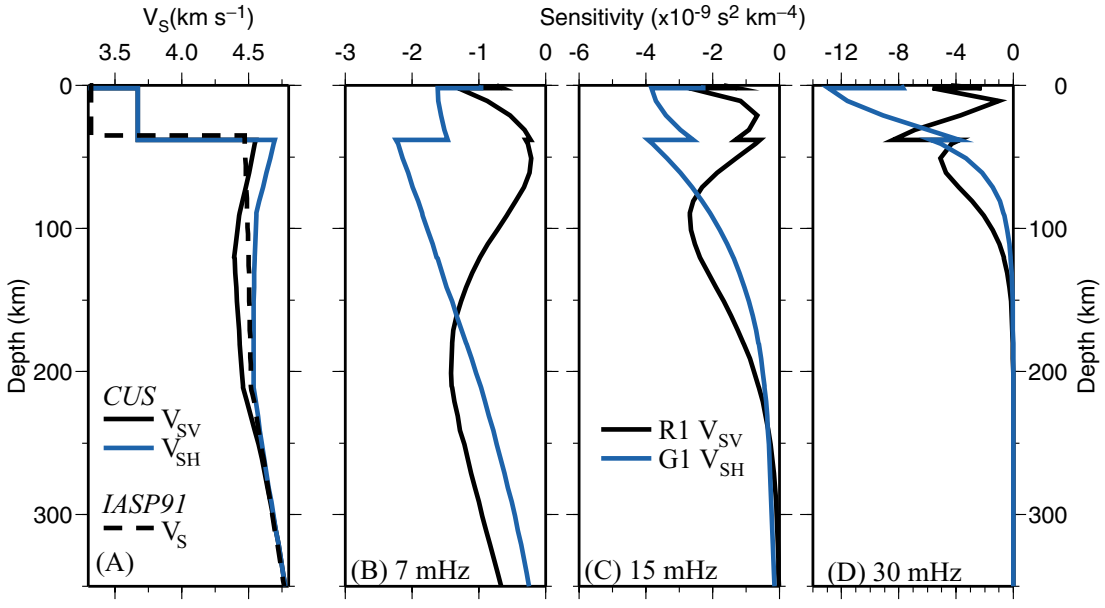

Figure 4. (a) Shear velocity model CUS, with v_{SH} shown in blue (grey) and v_{SV} shown in black. Radial anisotropy in CUS is ∼3 per cent. Also shown is the shear wave profile for IASP91 (dashed line), which served as a reference model for the CUS inversion. CUS in turn serves as the reference model for subsequent 2-D modelling of anisotropy beneath MOMA. (b)–(d) Representative partial derivative kernels for fundamental-mode Rayleigh (black) and Love (blue or grey) phase delays as a function of depth, for three different frequencies. Reference model for all kernels is CUS; kernels shown all correspond to observations at MM09 from the 950828 event. The kernels are with respect to the most sensitive model parameter for each wave type, i.e. the Rayleigh wave kernel is for v_{SV} and the Love wave kernel is for v_{SH}. These kernels give a feel for the depth sensitivity of the phase-delay observations at the different frequencies, with higher frequencies sensitive to shallower depths. Rayleigh waves sample deeper than Love waves at the same frequency. The kernels are negative because an increase in velocity leads to a decrease in phase delay (traveltime). (b) Kernels for observations with centre frequency of 7 mHz, which are sensitive well into the asthenosphere. (c) Kernels for 15-mHz observations, which are sensitive primarily to the lithosphere. (d) Kernels for 30-mHz observations, which are most sensitive to crustal structure.

sublithospheric LVZ. The piecewise continuous character of IASP91 was retained. Using this radially anisotropic reference model, we recalculated synthetic seismograms and remeasured the full set of delay times. The variance in the remeasured data was reduced by 77 per cent.

The phase delays relative to CUS are presented in Figs 5 and 6 for all data with acceptable S/N ratio. The times are grouped by centre frequency and at each frequency they are plotted as a function of distance along the array from west to east. A distance of zero corresponds to CCM and the largest distance near 16° corresponds to HRV, while a positive phase delay indicates an observation that is late relative to the arrival time predicted by the synthetic data. A number of conclusions can be drawn from these plots. First, the scatter in the observations is substantial at the lowest frequencies. Because 5–10 mHz surface waves have wavelengths (∼400–800 km) that are much larger than the station spacing (∼100 km), it is likely that this scatter is the result of measurement noise and the estimated standard errors assigned to the outliers are increased accordingly. Conversely, above 10 mHz the station-to-station variability is much smaller, providing confidence that these observations are not significantly affected by station noise. Secondly, the delay times from the two GoC events are generally larger (more positive) than those from the Texas event. This indicates substantially lower upper-mantle velocities along the ray path segments between the GoC and west Texas, consistent with tomographic models from the region (Fig. 2). Finally, the delay times of both Love and Rayleigh waves show a subtle decrease with increasing distance along the array, indicating that subarray velocities are higher than those of the reference model. For the Rayleigh wave observations, this trend appears to flatten out at along-array distances greater than ∼10° (Fig. 4, 7–25 mHz), implying lower velocities beneath the Appalachians and margin.

The choice of these three events allowed us to employ an array-based analysis scheme (Freybourger *et al.* 2001) that concentrates our sensitivity to anisotropic structure beneath the MOMA transect. Assuming that the individual source–receiver paths travel a common great-circle azimuth, then the delay time to the first station is sensitive to source location, origin time and structure outside the array, while variations in delay time along the array reflect structure beneath it. This assumption is not strictly true for these events, as they all lie slightly south of the great circle defined by the array. Two considerations imply that the geometry is close enough for an array analysis. First, the station-to-station variations from the two GoC events track each other very closely (for example, in the last panel of Fig. 5). Because the epicentres are slightly separated, the ray paths from the two events to a common station are furthest apart near the source. The fact that the interstation variation is so similar between the events implies that this variation is the result of common structure near the receivers. Secondly, the 3-D sensitivity kernels (e.g. Zhao *et al.* 2000) for observations considered here have across-path widths of the order of several hundred km. Baig *et al.* (2003) find that the maximum width of the 3-D kernel scales with the square root of the wavelength times the path length, which corresponds to widths ranging from 300–800 km for even the highest frequency (40 mHz) observations. The kernels for nearby stations thus strongly overlap outside of the array.

We establish three structural regimes for modelling these phase-delay observations. Two path models characterize the structure west of CCM and they are constrained by the mean phase delays for each event. The phase-delay trends across the array are modelled for

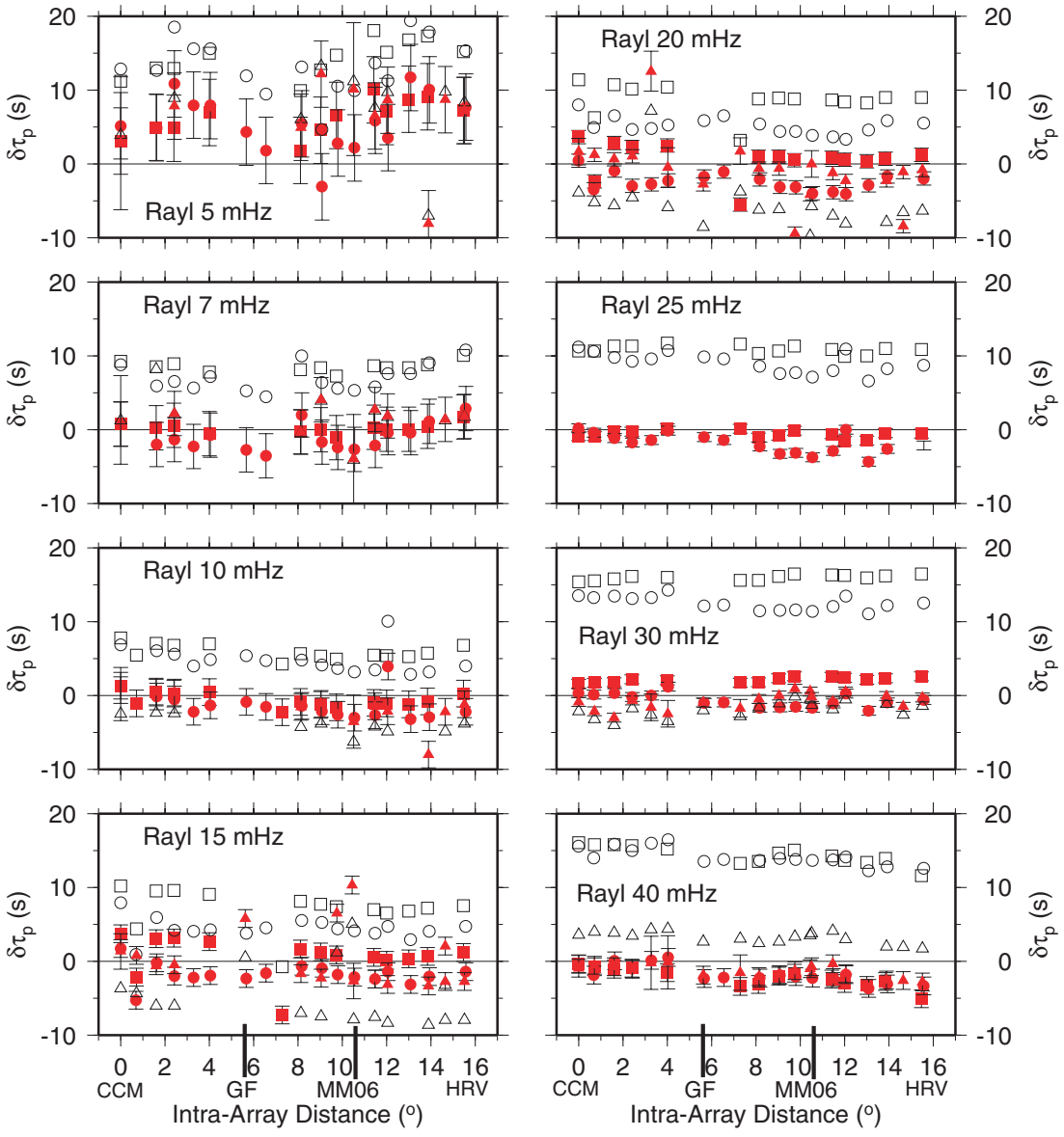

Figure 5. Frequency-dependent phase delays (traveltimes) of all observed fundamental-mode Rayleigh waves relative to model CUS, plotted as a function of distance along the array (from CCM). Open symbols represent raw observations from each event, while solid (red) symbols represent these data after they have been corrected for structure outside the array by subtracting the delay that accumulates between each event and the first station (CCM), using the path models shown in Fig. 7. Error bars represent *a priori* estimates based on seismogram S/N ratio level and frequency, and range from ∼8 s at low frequency to 1.5 s at high frequency. Squares correspond to delay times for event 950630, circles to event 950828 and triangles to event 950414. Horizontal line marks a phase delay of zero. Each panel presents observations at a specified frequency, ranging from 5 to 40 mHz, as labelled in each panel. Location of Grenville Front (GF) and station MM06 are marked.

subarray structure. This modelling takes two forms. In the first, we invert the phase-delay observations for radially anisotropic models of the upper mantle. In the second, we construct models of azimuthal anisotropy that are based on the shear wave splitting results of Fouch *et al.* (2000) and on estimates of intrinsic peridotite elasticity. Using the sensitivity kernels for our observations, we evaluate by forward modelling whether these splitting-derived models can satisfy the surface wave data.

3 INVERSE MODELS OF RADIAL ANISOTROPY

We inverted the phase-delay data for 2-D models of radial anisotropy using a linearized least-squares procedure (Freybourger *et al.* 2001). Radial anisotropy represents the simplest parametrization that can satisfy the Love/Rayleigh discrepancy (e.g. Dziewonski & Anderson 1981; Gaherty *et al.* 1999). The resulting models are transversely isotropic and thus cannot explain the shear wave splitting data, but they provide a means to quantify the depth distribution of the anisotropic structure affecting the surface waves (Gaherty *et al.* 1999). The 2-D model space contains four spherically symmetric structures (Fig. 2): a path model from the GoC events to CCM (PM1); a path model from the West Texas event to CCM (PM2); and a subarray model that includes a cratonic portion from CCM to MM06 (CRTN) and a margin portion from MM06 to HRV (MRGN). The models consist of eight layers between the Moho and 300-km depth, with linear changes in velocity within each layer and continuity required across layer boundaries. The crust contains two layers;

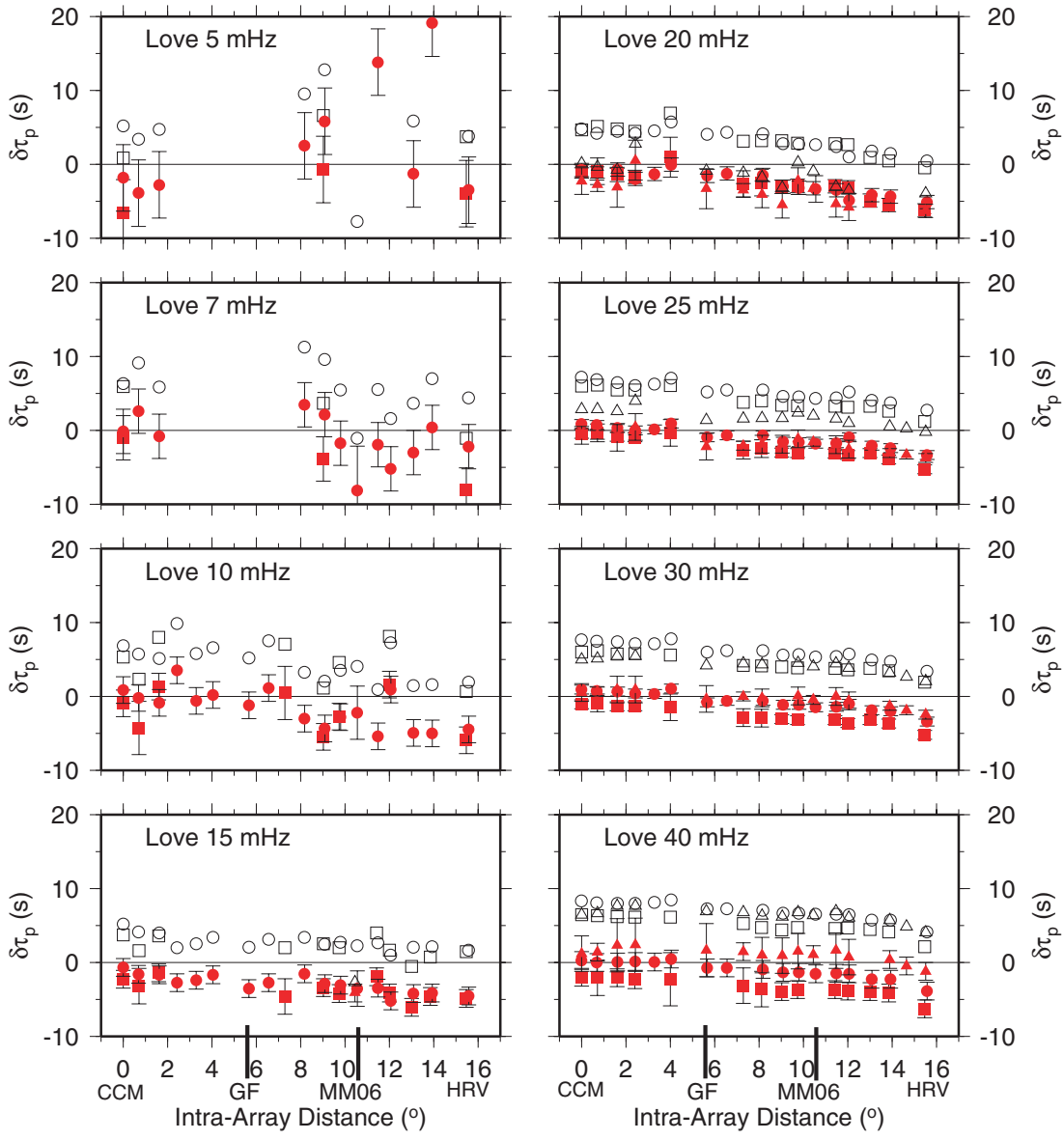

Figure 6. Same as Fig. 5, but for fundamental-mode Love waves.

for PM1 and PM2 the velocity and thickness of these layers are fixed using model Crust2.0 (Laske *et al.* 2001), while beneath the array the crustal parameters are required to satisfy the mean v_P, v_P/v_S and crustal thickness estimates from Li *et al.* (2002). Each model consists of the five parameters of radial anisotropy (v_{PH}, v_{PV}, v_{SH}, v_{SV} and η; e.g. Dziewonski & Anderson 1981). Our surface wave data are most sensitive to v_{SV} and v_{SH}, so we focus on these parameters. The four structures (PM1, PM2, CRTN and MRGN) are nominally independent, although nearly identical model and damping parameters ensure that the structures are similar.

We find that a suite of models fit the data equally well. Therefore, we utilize a hypothesis testing approach to evaluate the characteristics of these models that are necessary to fit the data (Gaherty & Jordan 1995; Gaherty *et al.* 1996). We focus on tests associated with the distribution of seismic anisotropy along the paths. Several hypotheses are considered:

(i) the upper 300 km of the mantle beneath the region is isotropic (i.e. $v_{PH} = v_{PV}$, $v_{SH} = v_{SV}$, $\eta = 1$);

(ii) anisotropy is limited to a region between the Moho and a lower boundary located between 100- and 180-km depth (i.e. the lithosphere is anisotropic);

(iii) anisotropy is limited to a region deeper than a boundary between 100- and 180-km depth (i.e. the asthenosphere is anisotropic);

(iv) anisotropy is required throughout the upper 300 km.

We also test our restriction to continuous structures by allowing for abrupt discontinuities in both isotropic and/or anisotropic structure. Possible discontinuities include the base of the lithosphere and/or LVZ (the G and L discontinuities, respectively; Revenaugh & Jordan 1991), and could have isotropic and anisotropic signatures (Gaherty *et al.* 1999). Evidence of L has been found beneath the eastern portion of MOMA and has been interpreted as the base of an isotropic LVZ (Li *et al.* 2002). These tests were performed independently for each portion of the model space (PM1, PM2, CRTN and MRGN). In all cases, goodness of fit was evaluated from formal estimates of normalized chi-squared and variance reduction, as well as by visual inspection of the fit to the along-array trends in phase delay (e.g.

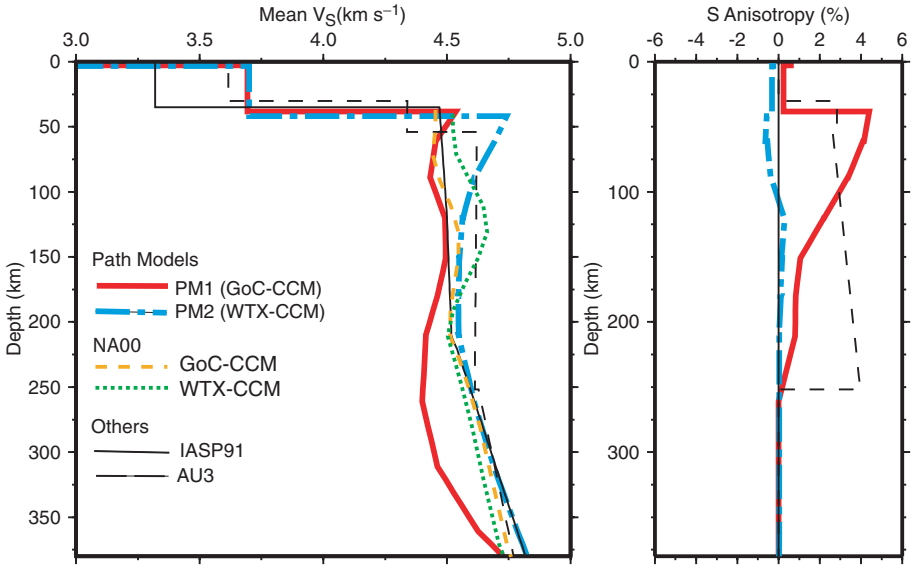

Figure 7. Radially anisotropic shear velocity structure of path models PM1 (thick red solid curves) and PM2 (thick blue dashed-dotted curves). Shown for comparison are the path averages through 3-D model NA00 (van der Lee 2002) for GoC-to-CCM (thick orange dashed curve) and WTX-to-CCM (thick green dotted curve), isotropic reference model IASP91 (thin black solid curve) and radially anisotropic model AU3 (thin black long-dashed curve) (Gaherty & Jordan 1995). Left panel displays mean shear speed ($v_S = (v_{SH} + v_{SV})/2$), while right panel displays shear anisotropy ($\Delta v_S = (v_{SH} - v_{SV})/v_S$ in per cent). PM1 is much slower than the more cratonic PM2 throughout the upper mantle. This velocity difference is similar to that found in NA00 above 150 km, but it persists to large depth in our models because of the strongly positive delay times at the lowest frequencies. Shear anisotropy in PM1 is strong above 150 km, but is small at greater depth. PM2 contains little anisotropy, but this is poorly resolved because of the weak Love waves for the Texas event.

Fig. 6), which is not necessarily captured by formal misfit estimates that are based on individual delay times. The models explain over 80 per cent of the variance relative to the intermediate reference model.

The preferred path models are shown in Fig. 7. PM1 is characterized by low velocities associated with propagation across the tectonically active GoC and Sonora region of Mexico. Radial anisotropy is strong at shallow (<150 km) depth, while at greater depths it is weaker, and the velocities are very slow to depths of at least 350 km. PM2 is characterized by higher mean shear velocities and the lithosphere is nearly isotropic. This apparent isotropy is not well constrained as a result of weak Love waves from the Texas event, but it is nonetheless consistent with the high-frequency waveform model of Rodgers & Bhattacharyya (2001). The shear velocity contrast between PM1 and PM2 is consistent with that in NA00 above 150-km depth (van der Lee 2002). The primary purpose of the path models is to account for structure outside the array in the traveltime data, and PM1 and PM2 are moderately successful in doing so. Figs 5 and 6 show the traveltime data for each event corrected for the appropriate path model (PM1 or PM2). If these corrections were perfect, the data from the three events would overlie each other and they would have a delay time of zero at CCM. The observations at 5 mHz indicated that velocities in PM1 are still slightly overestimated (despite the very low velocities in PM1), but at other frequencies the residuals at CCM and most traveltime differences between events are within the observational error.

Fig. 8 displays the mean shear velocity and shear anisotropy for the preferred subarray models. CRTN is characterized by high shear velocities, with mean v_S of order 4.55–4.65 km s^{-1} above approximately 180-km depth. A subtle LVZ is present near ∼200-km depth, but the mean shear velocities in this depth interval are still quite fast (∼4.5 km s^{-1}), much higher than in LVZs observed in oceanic and/or tectonic regions (including PM1), which have velocities of order 4.2–4.3 km s^{-1} (Gaherty *et al.* 1999). MRGN has shear velocities that are slower than CRTN by approximately 4 per cent through the upper 200 km, similar to the contrast found in tomographic models (Levin *et al.* 1999; van der Lee 2002; Li *et al.* 2003). The contrast is weakest near the surface and strongest near 150-km depth, consistent with a thin lithosphere beneath the margin (Menke & Levin 2002; van der Lee 2002).

Both models contain positive ($v_{SH} > v_{SV}$) shear anisotropy to 260-km depth, with a value of ∼4 per cent near the surface decaying to ∼2 per cent at 210 km (Fig. 8). Alternative models in which the anisotropy is limited to depths greater than 120 km (i.e. the lithosphere is isotropic) cannot satisfy the data. Fig. 9 presents a representative example in which the CRTN model is required to be isotropic: such a model fails to fit the strong trends in Love wave phase delays at intermediate periods. The anisotropy is weaker below 150 km in both CRTN and MRGN; this characteristic is present for all inversion results where anisotropy is allowed to extend deeper than 180 km, suggesting that the strongest anisotropy is in the lithosphere. The magnitude of this negative anisotropy gradient and the slightly steeper negative anisotropy gradient in MRGN are not well resolved. The maximum depth to which anisotropy extends is poorly constrained; the anisotropy could terminate as shallow as ∼180 km, or it may continue throughout the upper mantle (e.g. Gung *et al.* 2003). Furthermore, the presence of an isotropic and/or anisotropic L discontinuity (Gaherty & Jordan 1995; Li *et al.* 2002) cannot be resolved. The range of models that fit the data equally well provides rough bounds on model errors. For the subarray models, mean shear velocities are estimated to within approximately ±0.03 km s^{-1} and shear anisotropy is resolved to within approximately ±1 per cent. Below 250 km, the models are constrained by relatively noisy low-frequency observations and the model errors are approximately twice as large.

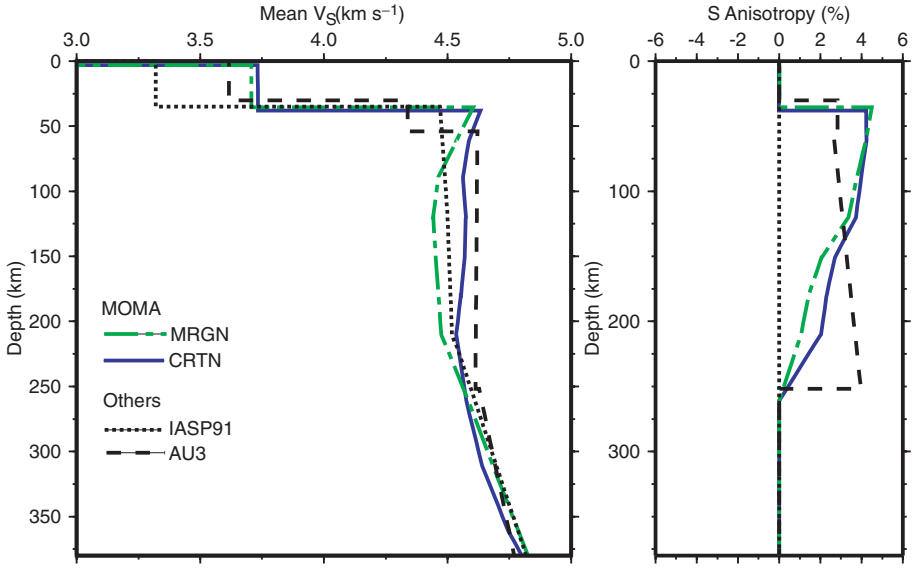

Figure 8. Radially anisotropic shear velocity models of upper-mantle structure beneath MOMA, derived from inversion of surface wave delays. Left panel displays mean shear speed ($v_S = (v_{SH} + v_{SV})/2$), while right panel displays shear anisotropy ($\Delta v_S = (v_{SH} - v_{SV})/v_S$ in per cent). Blue solid curves (CRTN) correspond to the average structure beneath the craton, corresponding to the region between stations CCM and MM06, while green dashed-dotted curves (MRGN) represent the structure beneath the margin, from MM06 to HRV. Shown for comparison are isotropic reference model IASP91 (dotted) and radially anisotropic model AU3 (dashed) (Gaherty & Jordan 1995). Radial anisotropy appears to be stronger than in AU3 at depths shallower than ∼100 km, but is somewhat weaker than AU3 below ∼150 km.

4 FORWARD MODELS OF AZIMUTHAL ANISOTROPY

The shear wave splitting results of Fouch *et al.* (2000) (Fig. 1) provide localized estimates of azimuthal anisotropy along the array. This anisotropy most likely arises from LPO in peridotite rocks, in which case the fast splitting direction corresponds to the dominant azimuth of the olivine *a* axes and the splitting time represents an integral of the shear velocity difference over depth (e.g. Silver 1996). Assuming that the peridotite elasticity in this region is comparable to that observed in petrofabric analyses of ophiolite outcrops and/or xenolith samples, a splitting time of 0.9 s implies an anisotropic layer with thickness of 100–250 km. The lower thickness limit corresponds to local shear wave anisotropy that is relatively strong (∼4 per cent), like that observed in ophiolites and xenoliths from oceanic environments (e.g. Christensen 1984; Kawasaki & Kon'no 1984; Nicolas & Christensen 1987; Ben Ismail & Mainprice 1998). A thicker layer is necessary if the local elastic anisotropy is weaker (∼2 per cent), such as that observed in xenoliths from continents (Ben Ismail & Mainprice 1998; Ben Ismail *et al.* 2001).

Our goal is to find a 2-D model of azimuthal anisotropy that satisfies the shear wave splitting data at each MOMA station, as well as the surface wave delay times observed across the array. We construct 2-D models that represent four scenarios for the distribution of azimuthal anisotropy beneath MOMA (Table 1). Along the array axis, the models are constructed of blocks centred beneath each of the 19 stations; the blocks are roughly 100-km wide, depending on station spacing. Within each block, the shear wave splitting fast direction from the associated station is used to specify the orientation of the local elasticity tensor. The thickness of the layer and the elastic parameters (other than orientation) are held constant along the array and the thickness is chosen to produce 0.9 s of splitting at all stations for each elasticity tensor. While the radial anisotropy found in the MRGN and CRTN models strongly suggest that the anisotropy must be located in the lithosphere, for completeness we also consider models where the anisotropy is confined to the asthenosphere (Table 1). Using the surface wave partial derivative kernels (Fig. 4) and first-order perturbation theory (Montagner & Nataf 1986), we then evaluated these models by calculating their predicted phase-delay behaviour for Rayleigh and Love waves propagating along the array.

Fig. 10 presents the path-corrected Love and Rayleigh wave phase-delay observations relative to an isotropic reference model (the isotropic average of CUS) at several frequencies, along with predicted phase-delay behaviour of the splitting-derived models from Table 1. The model predictions fail to match the data. In particular, while the predictions fall close to the scatter of the Rayleigh delays, the predicted Love delays are systematically too slow. This misfit is clear for models in which the anisotropy is located in the lithosphere, as well as models that are anisotropic in the asthenosphere but with an isotropic lithosphere.

This negative result is not surprising. The 2-D azimuthally anisotropic models have fast directions that are nearly parallel to the array. In peridotite-based models such as these, the speed of Rayleigh waves propagating parallel to the fast direction are enhanced relative to Love waves and the LR discrepancy in this direction is predicted to be small (e.g. Maupin 1985). In contrast, the observed LR discrepancy along the array is quite strong with Love waves anomalously fast (Fig. 10). The simplest way to produce an LR discrepancy like that observed is to orient olivine fast axes horizontal and highly oblique to the propagation direction, but such a model fails to match the splitting data. Models in which the fast axis is rotated out of the horizontal plane (i.e. a dipping fast axis) can satisfy the splitting, but would further decrease the Love speeds and thus fail to fit the LR discrepancy. Alternative single-layer models exist that could fit both the surface wave and splitting data. For instance, an orthorhombic structure with a slow axis oriented subvertically, with two independent fast directions oriented subhorizontally,

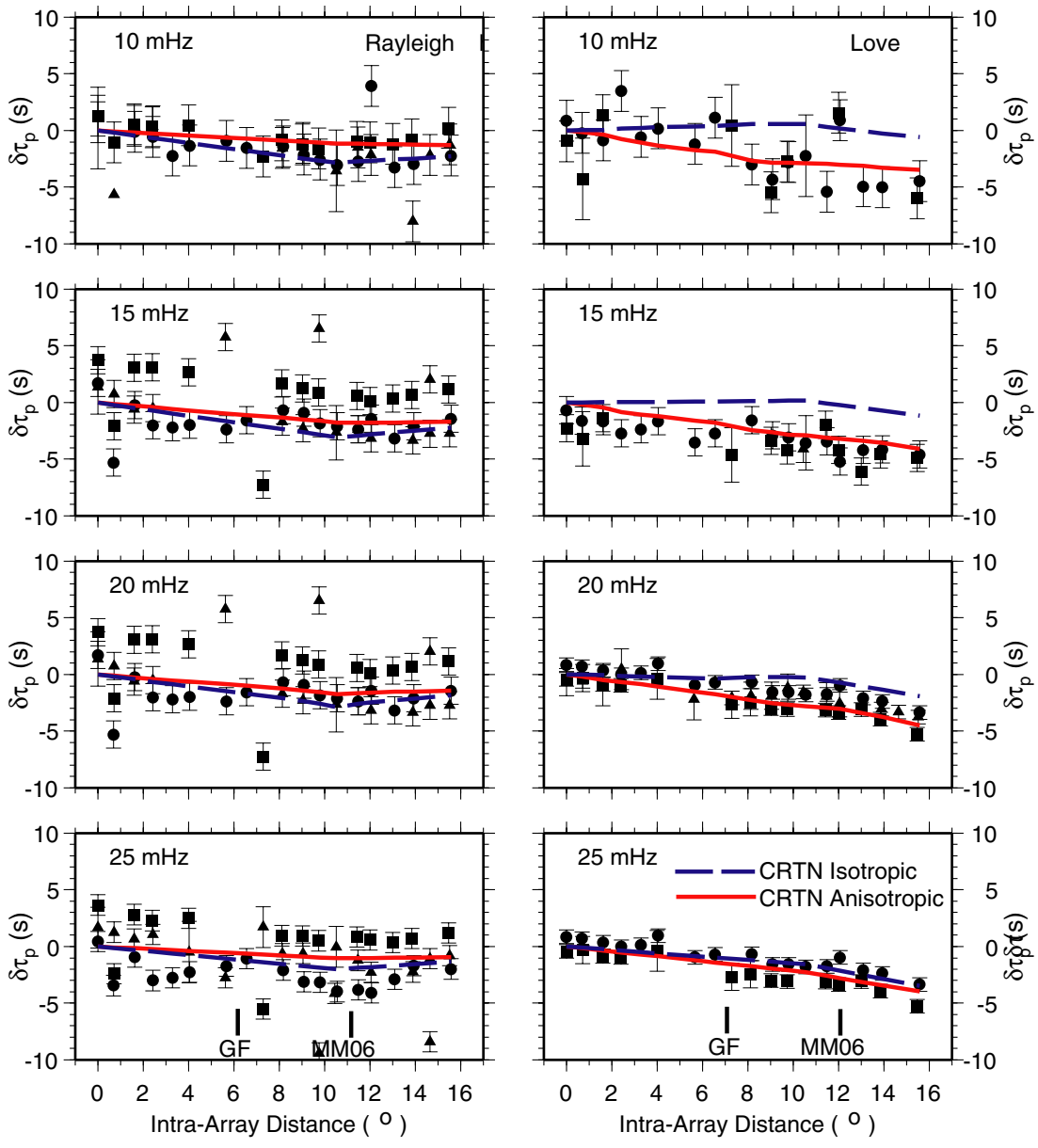

Figure 9. Fit of MOMA 2-D model from Fig. 8 to a subset of the phase-delay observations, specifically those observations most sensitive to structure between the Moho and 200-km depth (10–25 mHz). Solid symbols represent the observations relative to the radially anisotropic starting model CUS, corrected for structure outside the array by subtracting the delays associated with the path models. Squares correspond to delay times for event 950630, circles to event 950828 and triangles to event 950414. Color curves represent predicted phase delays for the preferred MOMA models shown in the Fig. 8 (solid red line), as well as an alternative model where the cratonic lithosphere is required to be isotropic (dashed blue line). Rayleigh wave delay times are plotted on the left and Love wave delays are on the right. Location of Grenville Front (GF) and station MM06 are marked. The isotropic craton model clearly fails to satisfy the relatively high propagation velocity of the Love waves across the array.

would produce Love wave velocities that are fast relative to Rayleigh waves at any azimuth, including that corresponding to the fastest split shear wave. Such elasticities are unlike those associated with olivine, which generally have a distinct fast velocity and an intermediate velocity closer to the slower velocity (e.g. Nicolas & Christensen 1987; Zhang & Karato 1995; Ben Ismail & Mainprice 1998; Bystricky *et al.* 2000).

5 DISCUSSION

Taken together, the surface wave phase delays and shear wave splitting constraints suggest a two-layer model for upper-mantle anisotropy beneath eastern North America. The surface wave data require a relatively shallow anisotropic layer that probably reflects lithospheric processes. This is clearest beneath the craton, where the correspondence of the radial anisotropy with high mean shear velocities above 200-km depth implies that the anisotropy is associated with fabric emplaced during past tectonic events. The layer that produces shear wave splitting theoretically could be placed anywhere between the surface and the core–mantle boundary, but the strong correlation between the observed fast directions and models of plate-motion-induced flow implies an asthenospheric depth for this layer (Fouch *et al.* 2000). We focus our discussion on the nature of the lithospheric anisotropy.

Table 1. Azimuthally anisotropic forward models.

	Layer Depth (km)	Δv_S (per cent)[1]	Reference
Model 1	40–140	4.2	Kawasaki & Kon'no (1984)
Model 2	180–280	4.2	Kawasaki & Kon'no (1984)
Model 3	40–290	1.7	Ben Ismail *et al.* (2001)
Model 4	180–430	1.7	Ben Ismail *et al.* (2001)

[1]Percentage difference in the velocities of two vertically propagating shear waves in the anisotropic layer. All models are constructed to produce 0.9 s of total splitting.

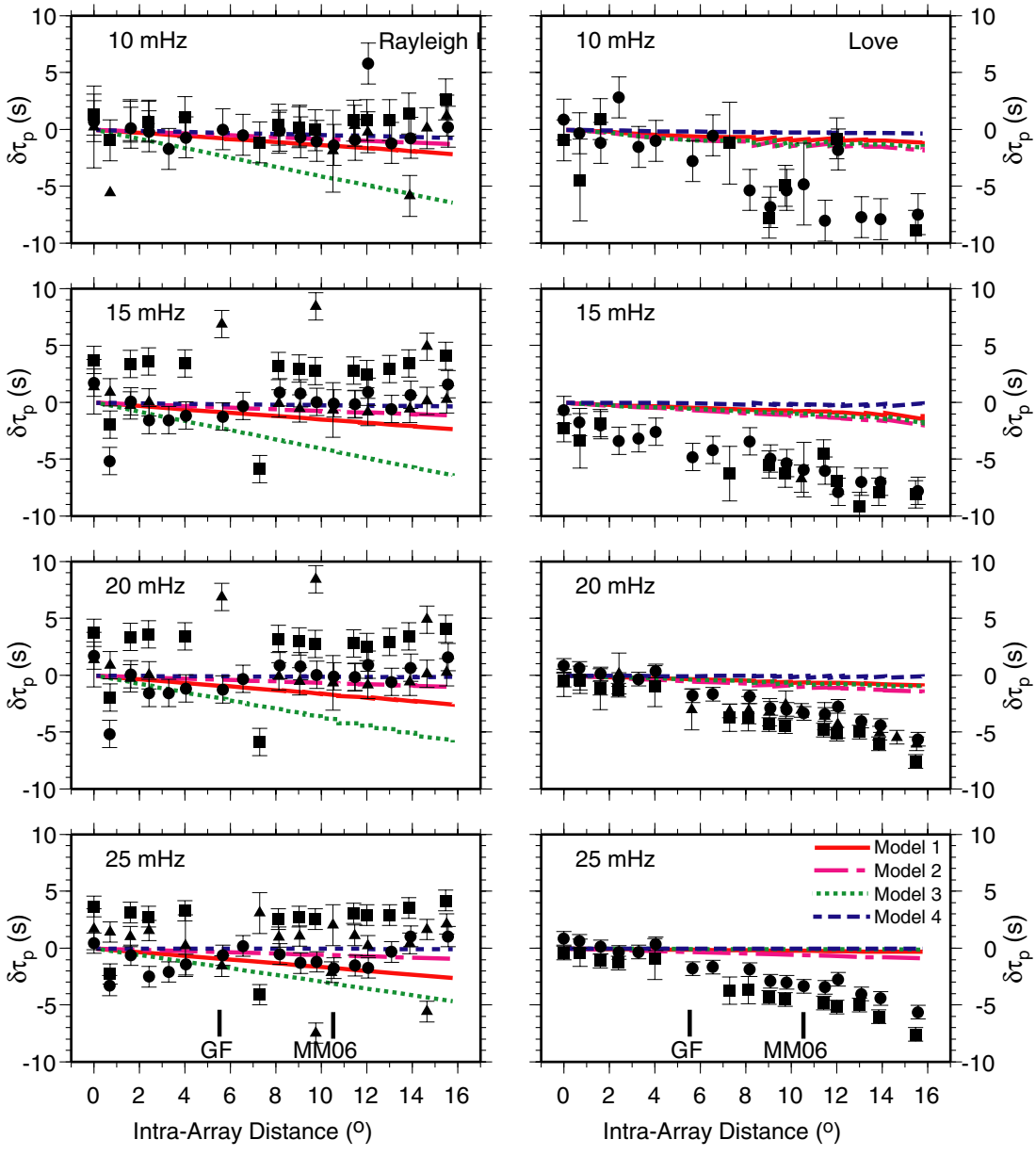

Figure 10. Evaluation of 2-D azimuthally anisotropic models constructed from the shear wave splitting results, using the phase-delay behaviour for Rayleigh (left panels) and Love (right panels) waves at the frequencies most sensitive to structure between the Moho and 200-km depth (10–25 mHz). Solid symbols represent the surface wave observations corrected for structure outside the array and referenced to the isotropic average of CUS, and curves represent predicted phase delays for the four different elastic structures from Table 1 (Model 1, red solid curve; Model 2, magenta dashed-dotted curve; Model 3, green dotted curve; Model 4, blue dashed curve). Location of Grenville Front (GF) and station MM06 are marked. Symbol types are the same is in Fig. 9.

The simplest model that we consider is suggested by the results of Levin *et al.* (2000), who proposed that the shear wave splitting observed at several stations in the margin region (including HRV and MM01–MM04) can be explained by two layers of anisotropy with fast directions oriented horizontal and oblique to the azimuth of the MOMA array. This class of model can satisfy the surface waves propagating across the margin because it significantly increases the velocity of Love waves relative to Rayleigh waves, and

if extended west to CCM it could explain the surface wave delays across the entire array. However, such a model is inconsistent with existing splitting observations. Multiple anisotropic layers produce shear wave splitting that is strongly dependent on the backazimuth of the event. Fouch *et al.* (2000) failed to find systematic backazimuth dependence in their observations at the MOMA stations and they opted for a single-layer interpretation. If their interpretation is incorrect, further analysis of additional splitting data from the region would be required to constrain the two-layer parameters along the entire length of the array.

Assuming that the Fouch *et al.* (2000) interpretation of the splitting data is correct, it suggests a more complex model in which the lithospheric structure produces the LR discrepancy but is relatively transparent to vertically propagating body waves. One possibility is that the lithosphere can be modelled as an isotropic laminate. In this model, the LR discrepancy is generated not by elastic anisotropy, but rather by strongly variable layered isotropic heterogeneity (Backus 1962). Such a model is unlikely. In order to produce apparent anisotropy of the magnitude found here, an isotropic laminate requires spatial fluctuations in isotropic velocities of order 12–16 per cent, much larger than the variation found among dominant mantle minerals (e.g. Gee & Jordan 1988; Jordan & Gaherty 1995).

The observed LR discrepancy can be explained by olivine LPO if the olivine fast axes are predominantly horizontal but vary in direction. If the variation in fast azimuth occurs over horizontal or vertical spatial scales that are substantially smaller than a seismic wavelength, numerical calculations indicate that no observable splitting would be produced in near-vertical broad-band shear waves, even if the intrinsic anisotropy is large (Rümpker & Silver 1998; Saltzer *et al.* 2000; Fischer *et al.* 2004). Furthermore, such models preserve the initial polarization of the incoming shear waves and thus do not erase splitting produced in deeper anisotropic regions (e.g. Saltzer *et al.* 2000; Fischer *et al.* 2004). A system in which the lithosphere is anisotropic with a fast direction that is quasi-horizontal and azimuthally variable over short-length scales and the asthenosphere is dominated by large-scale flow around the lithospheric keel, thus appears capable of satisfying both sets of observations. It is difficult to discern whether the lithospheric variations are predominantly horizontal or vertical. The remarkable lateral consistency of the MOMA splitting over relatively short scales ($\sim$100 km) and across distinct tectonic provinces (including the Grenville front) argue against purely horizontal heterogeneity (e.g. Fischer *et al.* 2004), but it cannot be precluded if the lateral variations occur over scale lengths $\ll$100 km. There is evidence for vertical heterogeneity beneath the margin in the form of the multilayer model advocated by Levin *et al.* (2000). If such vertical heterogeneity where more complex beneath the craton (e.g. the strong scattering regime of Saltzer *et al.* 2000), then it would satisfy the surface wave observations and still be transparent to shear wave splitting.

This suggestion of vertical anisotropic heterogeneity is similar to that found in other cratonic regions, notably Australia (Gaherty & Jordan 1995; Debayle & Kennett 2000a,b; Simons *et al.* 2002) and southern Africa (Freybourger *et al.* 2001). In these regions, radial anisotropy in the lithosphere is quite strong, but shear wave splitting is weak (e.g. Clitheroe & van der Hilst 1998; Silver *et al.* 2001) and/or non-existent (Ozalaybey & Chen 1999), and where observed it varies spatially and is inconsistent with the azimuthal anisotropy observed from surface waves (Freybourger *et al.* 2001; Simons *et al.* 2002). These observations are consistent with an anisotropic lithosphere that is dominated by quasi-horizontal olivine fabric with highly variable fast azimuth. In detail, there are intriguing differences between the observations in each region. Australia and eastern North America show evidence of coherent mantle fabric that is approximately consistent with the direction of apparent plate motion. In North America the splitting data provide this evidence, but in Australia it is only seen in the Rayleigh wave azimuthal anisotropy at depths of 200 km and greater (Debayle & Kennett 2000a; Simons *et al.* 2002). It is not clear whether the different splitting signature results from differences in asthenospheric structure (less effective generation of splitting in Australia), lithospheric structure (more effective scattering of split shear waves in Australia), or shear wave splitting data quality and coverage. Southern Africa is unique in that neither the splitting data nor the surface wave anisotropy suggest a component of anisotropy associated with plate motion. Instead, both appear consistent with anisotropy that is entirely located within the lithosphere (Freybourger *et al.* 2001; Silver *et al.* 2004). One possible explanation for this range of observations is that coherent splitting associated with plate motion requires a thick, weak asthenosphere. Splitting may be more coherent across the MOMA array in part because this portion of the North American craton is substantially younger and thus perhaps thinner (van der Lee 2002) than that in Australia (Simons *et al.* 2002) and southern Africa (Freybourger *et al.* 2001). A robust assessment of this hypothesis will require an evaluation of upper-mantle anisotropy in these and other regions using a comprehensive set of body and surface wave analyses.

The minimal change in anisotropy across the craton–margin transition is notable given the significant change in isotropic velocities (Fig. 8). In particular, the slower velocities between 100–200 km depth imply that much of the anisotropic zone beneath the margin is of order 100 K hotter than that beneath the craton (assuming $\delta v_P/\delta T$ of $-0.5\,\mathrm{m\,s^{-1}\,K^{-1}}$). This implies that much of the anisotropy beneath the margin is not lithospheric, but rather is associated with sublithospheric flow. The decorrelation between anisotropic and isotropic structure is also noted by Levin *et al.* (2000) and it suggests that the strength of the olivine fabric is not dependent on the present thermal or mechanical state of the mantle. In addition, the significant radial anisotropy inferred above 200 km beneath the margin contrasts with the lack of azimuthal anisotropy found from Rayleigh wave analyses from the same region (Menke & Levin 2002; Li *et al.* 2003). One explanation for this is that the shallow, asthenospheric anisotropy beneath the margin is dominated by small-scale structure as well.

6 CONCLUSIONS

We have investigated upper-mantle anisotropy beneath central and eastern North America by modelling the surface wave velocities traversing the length of the MOMA array. The mantle beneath MOMA is anisotropic from the Moho to at least 180-km depth. When parametrized as radial shear anisotropy, it has a magnitude of 2–4 per cent and this value is largely invariant across the transition from the craton to the margin. The surface wave velocities cannot be satisfied by a single-layer, 2-D model of azimuthal anisotropy constructed from the shear wave splitting results. The combined surface wave and splitting results appear to require at least two layers of anisotropy: a shallow, lithospheric layer that generates the surface wave anisotropy but is transparent to vertically propagating shear body waves and a deeper (presumably asthenospheric) layer that generates the shear wave splitting. One plausible model incorporates a lithosphere characterized by vertically heterogeneous anisotropic fabric, with underlying asthenospheric fabric aligned with plate-motion-induced flow. Complex lithospheric fabric has

been hypothesized for regions of weak and complex splitting (South Africa, Australia); evidence is accumulating that it may be appropriate for cratonic continental lithosphere in general.

ACKNOWLEDGMENTS

Seismic data were collected through the IRIS PASSCAL and GSN programs, and obtained from the IRIS Data Management Center (www.iris.edu). Figures were prepared using GMT (Wessel & Smith 1998). The author is thankful to K. Fischer and M. Fouch for helpful discussions, and S. van der Lee and A. Rodgers for providing models in electronic form. Thorough reviews by V. Levin, an anonymous referee, and Associate Editor R. van der Hilst led to substantial improvements in the manuscript. This work was supported by the US National Science Foundation. LDEO contribution number 6625.

REFERENCES

Alsina, D. & Snieder, R., 1995. Small-scale sublithospheric continental mantle deformation: constraints from SKS splitting observations, *Geophys. J. Int.,* **123,** 431–448.

Backus, G.E., 1962. Long-wave elastic anisotropy produced by horizontal layering, *J. geophys. Res.,* **67,** 4427–4440.

Baig, A.M., Dahlen, F.A. & Hung, S.-H., 2003. Traveltimes of waves in random 3-D media, *Geophys. J. Int.,* **153,** 467–482.

Barruol, G., Silver, P.G. & Vauchez, A., 1997. Seismic anisotropy in the eastern United States: Deep structure of a complex continental plate, *J. geophys. Res.,* **102,** 8329–8348.

Ben Ismail, W. & Mainprice, D., 1998. An olivine fabric database: an overview of upper mantle fabrics and seismic anisotropy, *Tectonophysics,* **296,** 145–157.

Ben Ismail, W., Barruol, G. & Mainprice, D., 2001. The Kaapvaal craton seismic anisotropy: petrophysical analyses of upper mantle kimberlite nodules, *Geophys. Res. Lett.,* **28,** 2497–2500.

Bystricky, M., Kunze, K., Burlini, L. & Burg, J.-P., 2000. High Shear Strain of Olivine Aggregates: Rheological and Seismic Consequences, *Science,* **290,** 1564–1567.

Christensen, N.I., 1984. The magnitude, symmetry, and origin of upper mantle anisotropy based on fabric analyses of ultramafic tectonites, *Geophys. J. R. ast. Soc.,* **76,** 89–111.

Clitheroe, G. & van der Hilst, R., 1998. Complex anisotropy in the Australian lithosphere from shear-wave splitting in broadband SKS records, in *Structure and Evolution of the Australian Continent*, Geodyn. Ser., Vol. 26, pp. 39–57, eds Braun J. *et al.,* American Geophysical Union, Washington, DC.

Debayle, E. & Kennett, B.L.N., 2000a. The Australian continental upper-mantle: Structure and deformation inferred from surface waves, *J. geophys. Res.,* **105,** 25 423–25 450.

Debayle, E. & Kennett, B.L.N., 2000b. Anisotropy in the Australasian upper mantle from Love and Rayleigh waveform inversion, *Earth planet. Sci. Lett.,* **184,** 339–351.

Dziewonski, A.M. & Anderson, D.L., 1981. Preliminary reference Earth model, *Phys. Earth planet. Int.,* **25,** 297–356.

Ekström, G. & Dziewonski, A.M., 1998. The unique anisotropy of the Pacific, *Nature,* **394,** 168–171.

Fischer, K., Li, A., Forsyth, D.W. & Hung, S.H., 2004. Imaging three-dimensional anisotropy with broad-band seismic arrays. In: *Seismic Data Analysis and Imaging with Global and Local Arrays.* AGU Geophysical Monograph, in press, 2004.

Forsyth, D.W., 1975. The early structural evolution and anisotropy of the oceanic upper mantle, *Geophys. J. R. astr. Soc.,* **43,** 103–162.

Fouch, M.J., Fischer, K.M., Parmentier, E.M., Wysession, M.E. & Clarke, T.J., 2000. Shear-wave splitting, continental keels, and patterns of mantle flow, *J. geophys. Res.,* **105,** 6255–6276.

Freybourger, M., Gaherty, J.B. & Jordan, T.H., 2001. Upper-mantle structure of the Kaapvaal craton from surface-wave analysis, *Geophys. Res. Lett.,* **28,** 2489–2492.

Gaherty, J.B. & Jordan, T.H., 1995. Lehmann discontinuity as the base of an anisotropic layer beneath continents, *Science,* **268,** 1468–1471.

Gaherty, J.B., Jordan, T.H. & Gee, L.S., 1996. Seismic structure of the upper mantle in a central Pacific corridor, *J. geophys. Res.,* **101,** 22 291–22 309.

Gaherty, J.B., Kato, M. & Jordan, T.H., 1999. Seismological structure of the upper mantle: A regional comparison of seismic layering, *Phys. Earth planet. Int.,* **110,** 21–41.

Gee, L.S. & Jordan, T.H., 1988. Polarization anisotropy and fine-scale structure of the Eurasian upper mantle, *Geophys. Res. Lett.,* **15,** 824–827.

Gee, L.S. & Jordan, T.H., 1992. Generalized seismological data functionals, *Geophys. J. Int.,* **111,** 363–390.

Gripp, A.E. & Gordon, R.G., 1990. Current plate velocities relative to the hotspots incorporating the NUVEL-1 global plate motion model, *Geophys. Res. Lett.,* **17,** 1109–1112.

Gung, Y., Panning, M. & Romanowicz, B., 2003. Global anisotropy and the thickness of continents, *Nature,* **422,** 707–711.

Jordan, T.H. & Gaherty, J.B., 1995. Stochastic modeling of small-scale, anisotropic structures in the continental upper mantle. In: *Proceedings of the 17th Annual Seismic Research Symposium*, PL-TR-95–2108, pp. 433–451, eds Lewkowicz, J.F. *et al.,* Phillips Laboratory, Massachusetts.

Kaminski, É. & Ribe, N., 2002. Time scales for the evolution of seismic anisotropy in mantle flow, *G-cubed,* **3,** 10.1029/2001GC000222.

Kawasaki, I. & Kon'no, F., 1984. Azimuthal anisotropy of surface waves and the possible type of the seismic anisotropy due to preferred orientation of olivine in the uppermost mantle beneath the Pacific Ocean, *J. Phys. Earth,* **32,** 229–244.

Laske, G., Masters, G. & Reif, C., 2001. *CRUST 2.0, A New Global Crustal Model at* 2 × 2 *Degrees,* http://mahi.ucsd.edu/Gabi/rem.html.

Levin, V., Menke, W. & Park, J., 1999. Shear wave splitting in the Appalachians and the Urals: a case for multilayered anisotropy, *J. geophys. Res.,* **104,** 17 975–17 987.

Levin, V., Menke, W. & Park, J., 2000. No regional anisotropic domains in the northeastern US Appalachians, *J. geophys. Res.,* **105,** 19 029–19 042.

Li, A., Fischer, K.M., van der Lee, S. & Wysession, M.E., 2002. Crust and upper-mantle discontinuity structure beneath eastern North America, *J. geophys. Res.,* **107,** 10.1029/2001JB000190.

Li, A., Forsyth, D.W. & Fischer, K.M., 2003. Shear velocity structure and azimuthal anisotropy beneath eastern North America from Rayleigh wave inversion, *J. geophys. Res.,* **108**(B8), 2362, 10.1029/2002JB002259.

Maupin, V., 1985. Partial derivatives of surface-wave phase velocities for flat anisotropic models, *Geophys. J. R. astr. Soc.,* **83,** 379–398.

Menke, W. & Levin, V., 2002. Anomalous seward dip of the lithosphere-asthenosphere boundary beneath northeastern USA detected using differential-array measurements of Rayleigh waves, *Geophys. J. Int.,* **149,** 413–421.

Montagner, J.-P., 2002. Upper mantle low anisotropy channels below the Pacific Plate, *Earth planet. Sci. Lett.,* **202,** 263–274.

Montagner, J.-P. & Nataf, H.C., 1986. A simple method for inverting the azimuthal anisotropy of surface waves, *J. geophys. Res.,* **91,** 511–520.

Montagner, J.-P. & Tanimoto, T., 1991. Global upper-mantle tomography of seismic velocities and anisotropy, *J. geophys. Res.,* **96,** 20 337–20 351.

Montagner, J.-P., Griot-Pommera, D.-A. & Lave, J., 2000. How to relate body wave and surface anisotropy?, *J. geophys. Res.,* **105,** 19 015–19 027.

Nicolas, A. & Christensen, N.I., 1987. Formation of anisotropy in upper mantle peridotites: A review, in, *Composition, Structure, and Dynamics of Lithosphere-Asthenosphere System*, Geodyn. Ser., Vol. 16, pp. 111–123, eds Fuchs, K. & Froidevaux, C., American Geophysical Union, Washington, DC.

Nolet, G., van Trier, J. & Huisman, R., 1986. A formalism for nonlinear inversion of seismic surface waves, *Geophys. Res. Lett.,* **13,** 26–29.

Ozalaybey, S. & Chen, W.-P., 1999. Frequency-dependent analysis of SKS/SKKS waveforms observed in Australia: evidence for null birefringence, *Phys. Earth planet Int.,* **114,** 197–210.

Revenaugh, J.S. & Jordan, T.H., 1991. Mantle layering from *ScS* reverberations, 3, The upper mantle, *J. geophys. Res.,* **96,** 19 781–19 810.

Ribe, N.M., 1992. On the relation between seismic anisotropy and finite strain, *J. geophys. Res.,* **97,** 8737–8747.

Rodgers, A. & Bhattacharyya, J., 2001. Upper mantle shear and compressional velocity structure of the Central US craton: shear-wave low-velocity zone and anisotropy, *Geophys. Res. Lett.,* **28,** 383–386.

Rümpker, G. & Silver, P.G., 1998. Apparent shear-wave splitting parameters in the presence of vertically varying anisotropy, *Geophys. J. Int.,* **135,** 790–800.

Saltzer, R., Gaherty, J.B. & Jordan, T.H., 2000. How are shear-wave splitting measurements affected by variations in azimuthal anisotropy with depth?, *Geophys. J. Int.,* **141,** 374–390.

Schulte-Pelkum, V., Masters, G. & Shearer, P.M., 2001. Upper mantle anisotropy from long-period P polarization, *J. geophys. Res.,* **106,** 21 917–21 934.

Shearer, P.M. & Orcutt, J.A., 1986. Compressional and shear wave anisotropy in the oceanic lithosphere—the Ngendei seismic refraction experiment, *Geophys. J. R. astr. Soc.,* **87,** 967–1003.

Silver, P.G., 1996. Seismic anisotropy beneath the continents: Probing the depths of Geology, *Ann. Rev. Earth planet. Sci.,* **24,** 385–432.

Silver, P.G. & Chan, W.W., 1991. Shear wave splitting and subcontinental mantle deformation, *J. geophys. Res.,* **96,** 16 429–16 454.

Silver, P.G. & Savage, M.K., 1994. The interpretation of shear-wave splitting parameters in the presence of two anisotropic layers, *Geophys. J. Int.,* **119,** 949–963.

Silver, P.G., Gao, S.S., Liu, K.H. & the Kaapvaal Seismic Group, 2001. Mantle deformation beneath southern Africa, *Geophys. Res. Lett.,* **28,** 2493–2496.

Silver, P.G., Fouch, M.J., Gao, S.S., Schmitz, M., & the Kaapvaal Seismic Group, 2004. Seismic anistropy, mantle fabric and the magmatic evolution of Precambrian Southern Africa, *African J. Geol.,* in press.

Simons, F.J. & van der Hilst, R.D., 2003. Seismic and mechanical anisotropy and the past and present deformation of the Australian lithosphere, *Earth planet Sci. Lett.,* **211,** 271–286.

Simons, F.J., van der Hilst, R.D., Montagner, J.-P. & Zielhuis, A., 2002. Multimode Rayleigh wave inversion for shear wave speed hetergeneity and azimuthal anistropy of the Australian upper mantle, *Geophys. J. Int.,* **151,** 738–754.

van der Lee, S., 2002. High-resolution estimates of lithospheric thickness from Missouri to Massachusetts, USA, *Earth planet Sci. Lett.,* **203,** 15–23.

Vinnik, L.P., Makeyeva, L.I., Milev, A. & Usenko, A.Y., 1992. Global patterns of azimuthal anisotropy and deformations in the continental mantle, *Geophys. J. Int.,* **111,** 433–447.

Vinnik, L.P., Green, R.W.E. & Nicolaysen, L.O., 1995. Recent deformations of the deep continental root beneath southern Africa, *Nature,* **375,** 50–52.

Wessel, P. & Smith, W.H.F., 1998. New, improved version of the Generic Mapping Tools released, *EOS, Trans. Am. geophys. Un.,* **79,** 579.

Yu, Y. & Park, J., 1994. Hunting for azimuthal anisotropy beneath the Pacific Ocean region, *J. geophys. Res.,* **99,** 15 399–15 421.

Zhang, S. & Karato, S.-I., 1995. Lattice preferred orientation of olivine in simple shear deformation and the flow geometry of the upper mantle of the Earth, *Nature,* **389,** 774–777.

Zhao, L., Jordan, T.H. & Chapman, C.H., 2000. Three-dimensional Fréchet differential kernels for seismic delay times, *Geophys. J. Int.,* **141,** 558–576.